Controlled Doping of Silicon Nanocrystals Investigated by Solution-Processed Field Effect Transistors

Ryan Gresback,[†] *Nicolaas J. Kramer,*[‡] *Yi Ding,*[†] *Ting Chen,*[§] *Uwe R. Kortshagen,*[‡]*

Tomohiro Nozaki[†]*

† Department of Mechanical Science and Engineering, Graduate School of Science and Engineering, Tokyo Institute of Technology, 2-12-1 Ookayama, Meguro-ku, Tokyo 152-8552, Japan; ‡ Department of Mechanical Engineering, University of Minnesota, 111 Church St SE, Minneapolis, MN 55455, United States; § Department of Chemical Engineering and Materials Science, University of Minnesota, 421 Washington Ave SE, Minneapolis, Minnesota 55455, United States

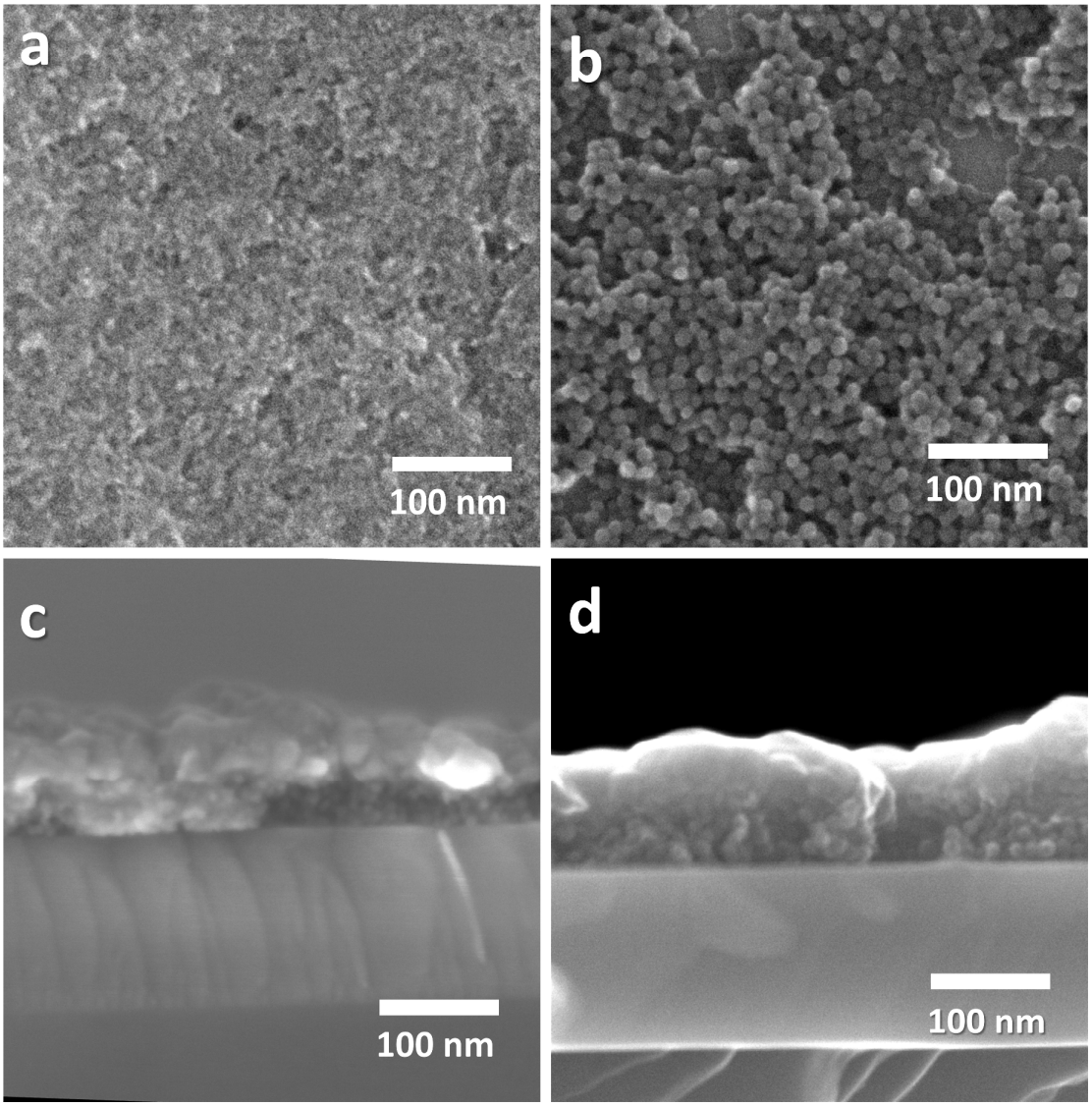

Figure S1: SEM images of Si NC FETs (a,b) top view and (c,d) cross-sectional view with sizes of (a,c) 4-7 nm and (b,d) 8-15 nm.

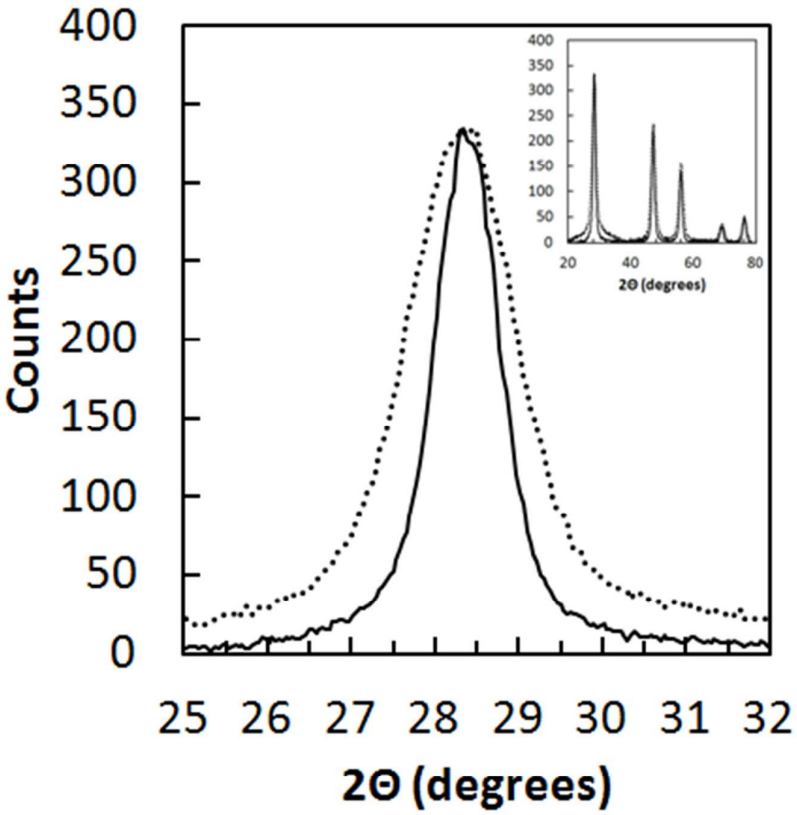

Figure S2: X-ray diffraction patterns of (solid) large and (dotted) small NCs for (111) reflection. Inset: full pattern. Extracted sizes for large: 9.3 nm ± 0.2 nm Small: 5.5 nm ± 0.1 nm

Transient processes

We observe three main transient processes, as highlighted in Figure S3, during measurements of the Si NC FETs: 1) time-dependent I_D at constant applied V_{GS} and V_{DS} [Figure S3(a)], 2) "off" current dependent on the sweep-rate of V_{GS}, and 3) a shift in V_T due to gate-bias stressing of the devices. We attributed these effects to the screening of the electric field by trapped carriers and defect creation/removal. The former mechanism is shown in Figure S3(a) where V_{GS} is suddenly changed and I_D is monitored as a function of time. Similar results have been observed for other NC FETs and this type of behavior is believed to originate either at the gate-oxide/NC interface or due to traps in the NCs.[1,2] Here

we cannot conclusively demonstrate either mechanism, however the transient response rate changes significantly for each batch of NCs which suggests similar trapping process related to the Si NC surface as previously described for 2-terminal conductivity measurements of Si NCs[3] and Si NC FETs.[4] Similar trapping processes are likely responsible for the "off" current that is dependent on the sweep-rate of V_{GS}, as shown in Figure S3b.

The shift in V_T can be exaggerated by holding a gate-bias for a period of time followed by a quick measurement of the I_D–V_{GS} characteristics. In Figure S3c typical I_D–V_{GS} characteristics are shown after a device has been stressed for a period of time with an applied gate voltage of $V_{GS} = V_{GD} = 30$ V. V_T shifts towards the applied stress bias and in Figure S3d the threshold voltage shift (ΔV_T) is plotted for several Si NC FETs fabricated with different doping concentrations and sizes. Here we did not observe any apparent trend in ΔV_T with size or doping-type and there were both significant variations between different NC batches and within the same batch across different devices. In addition to the trapping process previously highlighted, where deep traps could impact V_T, defect creation or removal is expected to also contribute to changes in V_T. In amorphous Si FETs this gate-bias induced shift of V_T is attributed to creation (positive gate bias) or removal (negative gate bias) of defects related to hydride species.[5,6] A similar effect would be expected for Si NCs due to the large amount of hydrogen terminating the NC surface and the relatively low energy required for rearrangement of Si-H_x bonds.[7] Other possibilities include mobile traps (for example metal ions) that can have a similar effect on V_T. These results demonstrate the need to quickly acquire the I_D–V_{GS} characteristics to accurately determine the carrier mobility and V_T without the interference of traps or defects. The origin of these traps or defects is presently unclear and further investigation is necessary.

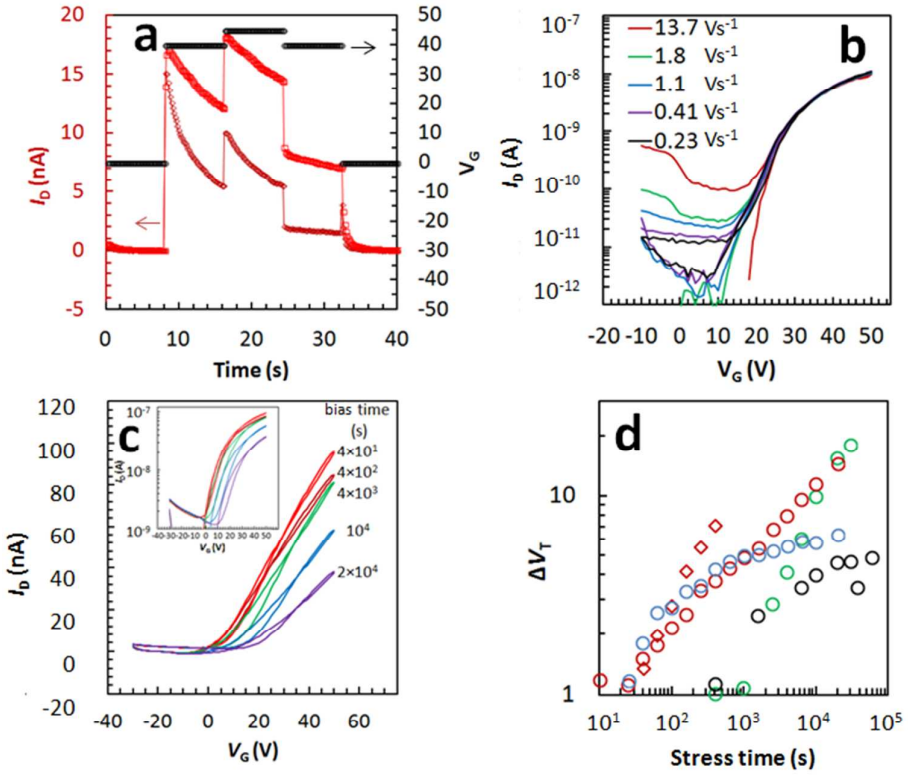

Figure S3: (a) Drain-current (red) with sudden changes in gate voltage (black circle) for (red squares and diamonds) two devices fabricated from 4-7 nm 1% B doped Si NCs. (b) I_D–V_{GS} characteristics for different V_{GS} sweep rates (see legend for sweep rates) for 8-15 nm 1% B doped. (c) I_D–V_{GS} characteristics for various gate stress times (see legend) for 8-15 nm 1% P doped with V_{DS} = 30 V and (d) ΔV_T with gate stress applied (V_{GS} = V_{GD} = 30 V) for (red diamonds) 4-7 nm 1% P doped, (red circles) 8-15 nm 1% P doped, and (black circle) 8-15 nm intrinsic, and (V_{GS} = V_{GD} = -30 V) for (blue circle) 1% B 8-15 nm and (green circles) 1% P 8-15 nm Si NC FETs.

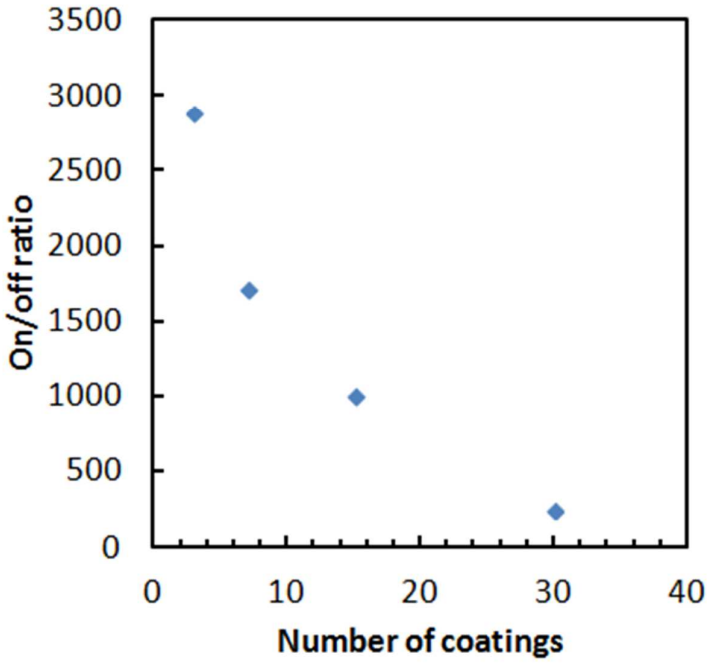

Figure S4: On/off ratio as a function of Si NC thickness for slow scan rate (0.1 Vs^{-1}) for 1% B doped 8-15 nm Si NC FET.

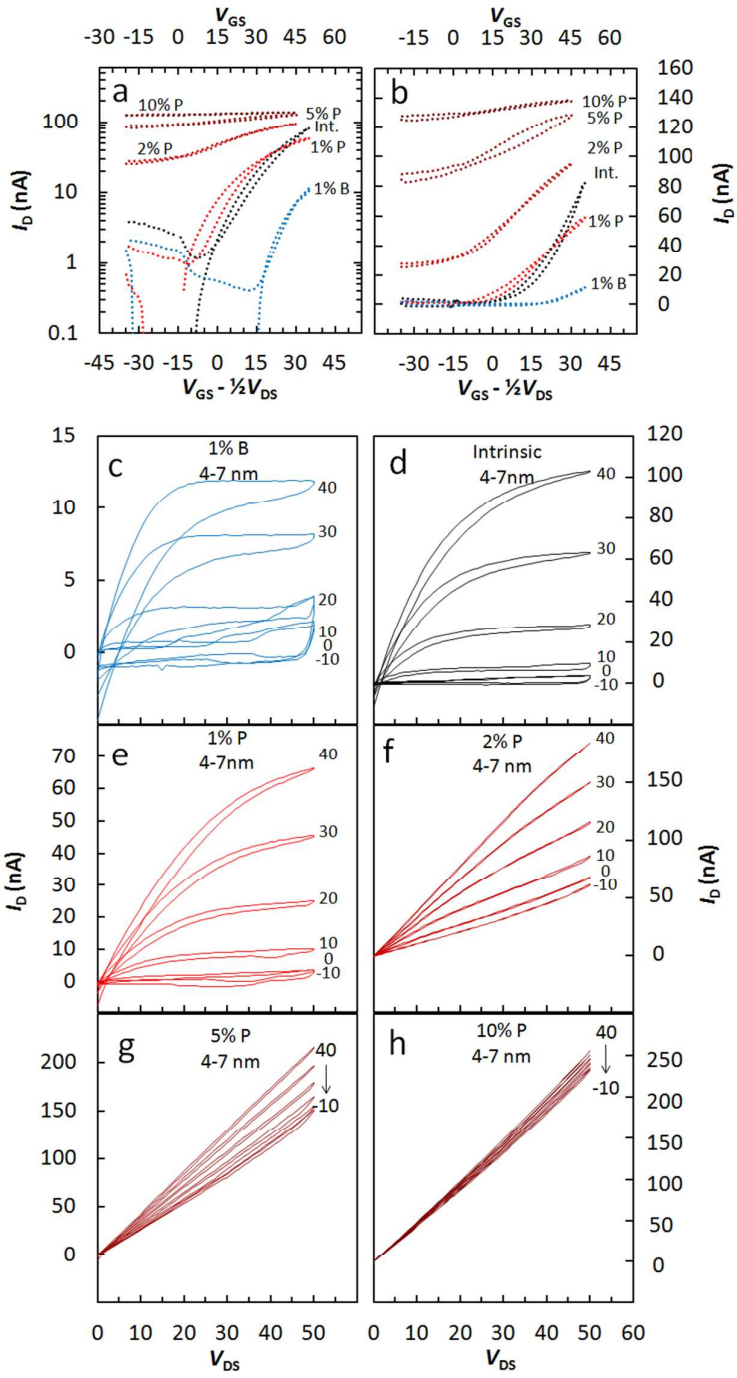

Figure S5: I_D-V_{GS} traces for small (4-7 nm) Si with various nominal doping concentrations (see legend), on a (a) semi-log scale (b) on a linear scale measured with a drain-source voltage (V_{DS}) of 30 V. Output characteristics of small (4-7 nm) Si NCs thin-film transistors of with nominally (c) 1% B doped, (d) intrinsic, (e) 1% P doped, (f) 2% P doped, (g) 5% P doped, and (h) 10% P doped. All devices shown have W/L of 2000/20 μm.

Threshold voltage

The threshold voltage (V_T) for a FET operating in *inversion* can be modeled with the gradual channel approximation (or Shockley model).[8,9] This is the common model used to describe metal-oxide-semiconductor FETs (MOSFETs), however many thin-film FETs (TFTs) can operate in both *inversion* and *accumulation* as there is no junction at the source/drain contacts. For the purposes of determining the dopant activation efficiency we assume B-doped Si NC FETs operate in inversion regime and P-doped Si NCs operate in the accumulation regime.

For devices in *inversion*, V_T is the sum of the flatband voltage (V_{FB}), twice the bulk potential of the Si NC film (ϕ_F), and depletion layer across the oxide,

$$V_T = V_{FB} + 2\phi_F + \frac{q(N_a - N_d)}{C_{ox}} \sqrt{\frac{2\varepsilon_s(2\phi_F + V_{SB})}{q(N_a - N_d)}},$$

where ε_s, q, N_a, N_d, V_{SB}, and C_{ox}, are the dielectric constant of the Si NC thin-film, charge of an electron, number density of acceptor and donor atoms, source-to-body voltage and oxide capacitance, respectively. The flatband voltage (V_{FB}) is given by,

$$V_{FB} = \Phi_{MS} - \frac{Q_f}{C_{ox}}.$$

With the fixed charge at the oxide (Q_f) assumed to be zero, and the difference between the workfunction of the gate material and Si NC film (Φ_{MS}), given by,

$$\Phi_{MS} = \Phi_M - \Phi_S = \Phi_M - \chi + \frac{E_g}{2} + \phi_F.$$

Where Φ_M is (~5.1 eV) for the *p*+ silicon substrate used in this study, X is electron affinity of the Si NC film (4.05 eV) and E_g is the bandgap of the Si NC thin-film (1.17 eV). The bulk potential of the Si NC film is given by:

$$\phi_F = \frac{kT}{q} \ln \frac{N_a}{n_i} \; and \; \phi_F = -\frac{kT}{q} \ln \frac{N_d}{n_i}.$$

Where k, T, and n_i, are the Boltzmann constant, temperature, and intrinsic carrier density (assumed as 10^{10} cm^{-3}).

For devices in *accumulation*, the channel is formed in the entire thickness h of the Si NC thin-film [assumed as 30 nm for Figure 4(a)] and the threshold voltage is related to the density of N_d and N_a: [8–10]

$$V_T = V_{FB} - \frac{qh(N_d - N_a)}{C_{ox}}.$$

Although we assume bulk-like properties for the Si NC thin-film, for devices in inversion size-dependent effects are expected to alter ε_s, X, and E_g. For the latter two material properties, X, and E_g, have been observed to be strongly coupled to each other with decreasing size[11] where we expect only a small change in V_T for Si NCs as compared to bulk silicon (<1 V). As the size of Si NCs is reduced ε_s has been observed to be strongly size-dependent where bulk Si is 11.9 and can be reduced up to 4.5 for small 2 nm Si NCs).[12,13] This is expected to reduce the change in V_T due to excess donors or electrons by $(\varepsilon_{s,bulk} - \varepsilon_{s,NC})^{-0.5}$ compared to bulk. This size-dependence cannot be accurately determined due to the large variation in doping efficiencies that is expected to result in similarly large variations in V_T.**FTIR Assignments**

The FTIR of Si NCs spectra are typical for this plasma synthesis method as shown in Figure S6 (normalized and linear baseline subtracted) and have been discussed in detail elsewhere.[14–15] Briefly, silicon hydride stretching modes (Si-H_x) are observed at 2140 cm^{-1}, 2100 cm^{-1}, 2080 cm^{-1} for x = 3, 2, 1, respectively. In addition silicon hydride deformation, scissor and wage modes at 960 cm^{-1}, 903 cm^{-1}, 863 cm^{-1} are assigned.[17] Oxide related features can also be seen at ~2250 cm^{-1} for O-Si-H_X[14,15,18] and 1040 cm^{-1}, and 1100 cm^{-1} for Si-O-Si bonds.[14,15,18] These oxide modes are generally much smaller as compared to the hydride modes revealing that the surface of the Si NCs is mostly hydrogen terminated. For chlorine terminated Si NCs, we attribute the broad feature at ~570 cm^{-1} to Si-Cl_x stretching and bending modes.[19–21] The broad absorbance for 10% P and B doped 10 nm Si NCs is characteristics of localized surface plasmon resonance (LSPR).[16] It should be noted that the

difference in doping concentration required to exhibit LSPR in Figure 6a compared to the previous report is attributed to different synthesis conditions resulting in different size and possibly activation of dopants.

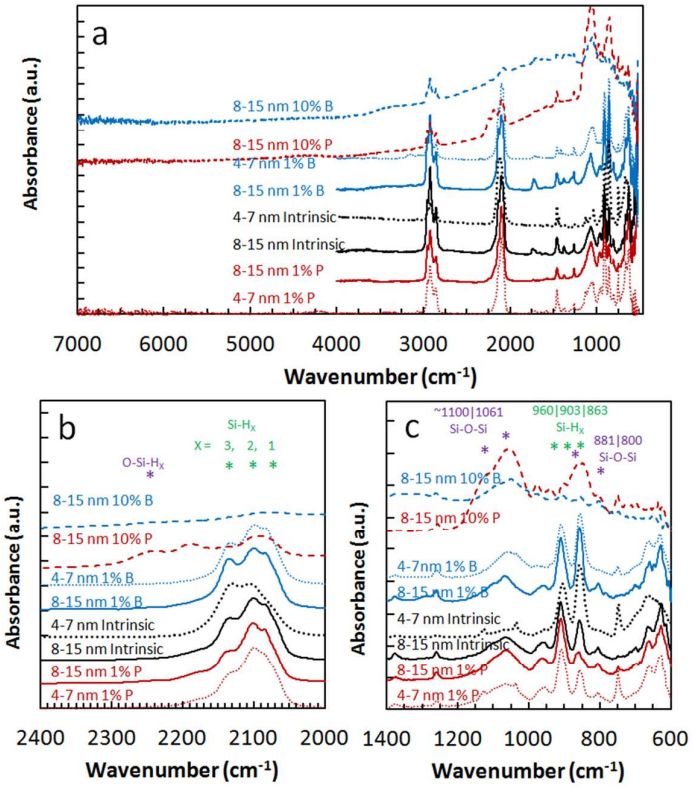

Figure S6: FTIR spectra of Si NCs for (a) full spectra, and (b,c) detailed regions. See figure for trace assignments.

Supplementary References

(1) Luther, J. M.; Law, M.; Song, Q.; Perkins, C. L.; Beard, M. C.; Nozik, A. J. Structural, Optical, and Electrical Properties of Self-Assembled Films of PbSe Nanocrystals Treated with 1,2-Ethanedithiol. *ACS Nano* **2008**, *2*, 271–280.

(2) Liu, Y.; Gibbs, M.; Puthussery, J.; Gaik, S.; Ihly, R.; Hillhouse, H. W.; Law, M. Dependence of Carrier Mobility on Nanocrystal Size and Ligand Length in PbSe Nanocrystal Solids. *Nano Lett.* **2010**, *10*, 1960–1969.

(3) Pereira, R. N.; Niesar, S.; You, W. B.; da Cunha, A. F.; Erhard, N.; Stegner, A. R.; Wiggers, H.; Willinger, M.-G.; Stutzmann, M.; Brandt, M. S. Solution-Processed Networks of Silicon Nanocrystals: The Role of Internanocrystal Medium on Semiconducting Behavior. *J Phys Chem C* **2011**, *115*, 20120–20127.

(4) Weis, S.; Körmer, R.; Jank, M. P. M.; Lemberger, M.; Otto, M.; Ryssel, H.; Peukert, W.; Frey, L. Conduction Mechanisms and Environmental Sensitivity of Solution-Processed Silicon Nanoparticle Layers for Thin-Film Transistors. *Small* **2011**, *7*, 2853–2857.

(5) Powell, M. J.; Deane, S. C.; Milne, W. I. Bias-stress-induced Creation and Removal of Dangling-bond States in Amorphous Silicon Thin-film Transistors. *Appl. Phys. Lett.* **1992**, *60*, 207–209.
(6) Deane, S. C.; Wehrspohn, R. B.; Powell, M. J. Unification of the Time and Temperature Dependence of Dangling-bond-defect Creation and Removal in Amorphous-silicon Thin-film Transistors. *Phys. Rev. B* **1998**, *58*, 12625–12628.
(7) Niesar, S.; Stegner, A. R.; Pereira, R. N.; Hoeb, M.; Wiggers, H.; Brandt, M. S.; Stutzmann, M. Defect Reduction in Silicon Nanoparticles by Low-Temperature Vacuum Annealing. *Appl. Phys. Lett.* **2010**, *96*, 193112.
(8) Sze, S. M.; Ng, K. K. *Physics of Semiconductor Devices*; John Wiley & Sons, 2006.
(9) Horowitz, G. Organic Field-Effect Transistors. *Adv. Mater.* **1998**, *10*, 365–377.
(10) Tecklenburg, R.; Paasch, G.; Scheinert, S. Theory of Organic Field Effect Transistors. *Adv. Mater. Opt. Electron.* **1998**, *8*, 285–294.
(11) Von Behren, J.; van Buuren, T.; Zacharias, M.; Chimowitz, E. H.; Fauchet, P. M. Quantum Confinement in Nanoscale Silicon: The Correlation of Size with Bandgap and Luminescence. *Solid State Commun.* **1998**, *105*, 317–322.
(12) Wang, L.-W.; Zunger, A. Dielectric Constants of Silicon Quantum Dots. *Phys. Rev. Lett.* **1994**, *73*, 1039.
(13) Zunger, A.; Wang, L.-W. Theory of Silicon Nanostructures. *Appl. Surf. Sci.* **1996**, *102*, 350–359.
(14) Mangolini, L.; Kortshagen, U. Plasma-Assisted Synthesis of Silicon Nanocrystal Inks. *Adv. Mater.* **2007**, *19*, 2513–2519.
(15) Pereira, R. N.; Rowe, D. J.; Anthony, R. J.; Kortshagen, U. Freestanding Silicon Nanocrystals with Extremely Low Defect Content. *Phys. Rev. B* **2012**, *86*, 085449.
(16) Rowe, D. J.; Jeong, J. S.; Mkhoyan, K. A.; Kortshagen, U. R. Phosphorus-Doped Silicon Nanocrystals Exhibiting Mid-Infrared Localized Surface Plasmon Resonance. *Nano Lett.* **2013**, *13*, 1317–1322.
(16) Marra, D. C.; Edelberg, E. A.; Naone, R. L.; Aydil, E. S. Silicon Hydride Composition of Plasma-deposited Hydrogenated Amorphous and Nanocrystalline Silicon Films and Surfaces. *J. Vac. Sci. Technol. Vac. Surfaces Films* **1998**, *16*, 3199–3210.
(18) Mawhinney, D. B.; Glass, J. A.; Yates, J. T. FTIR Study of the Oxidation of Porous Silicon. *J. Phys. Chem. B* **1997**, *101*, 1202–1206.
(19) Gresback, R.; Nozaki, T.; Okazaki, K. Synthesis and Oxidation of Luminescent Silicon Nanocrystals from Silicon Tetrachloride by Very High Frequency Nonthermal Plasma. *Nanotechnology* **2011**, *22*, 305605.
(20) Rivillon, S.; Chabal, Y. J.; Webb, L. J.; Michalak, D. J.; Lewis, N. S.; Halls, M. D.; Raghavachari, K. Chlorination of Hydrogen-terminated Silicon (111) Surfaces. *J Vac Sci Technol* **2005**, *23*, 1100–1106.
(21) Rivillon, S.; Amy, F.; Chabal, Y. J.; Frank, M. M. Gas Phase Chlorination of Hydrogen-passivated Silicon Surfaces. *Appl. Phys. Lett.* **2004**, *85*, 2583.